

# Ultra-Sensitivity Widefield, Confocal Surface Plasmon Interferometry Using Sequential Coding

Suejit Pechprasarn

*College of Biomedical Engineering, Rangsit University, Pathum Thani, Thailand*

**Keywords:** Surface Plasmon Resonance, Confocal Microscope, Molecular Binding, Optical Instrumentation.

**Abstract:** Interferometry has been a standard technique for optical phase measurement. Most single-molecule sensitivity measurements and imaging tools rely very much on the interferometric measurement of dual optical beams. We have developed an embedded confocal interferometric microscope and demonstrated by theoretical calculation that the system can achieve single molecule detection sensitivity. Of course, several challenges need to be addressed to achieve such ultra-sensitivity. The confocal surface plasmon microscope is a beam scanning system, and it also suffers from thermal variations due to long data acquisition time. Here we propose a widefield quantitative confocal surface plasmon interferometric microscope configuration using orthogonal coding. The proposed system sequentially illuminates a plasmonic sample with multiple focal points in the sample plane based on an orthogonal code such as a Hadamard code. The images of the illumination sequences are then captured and processed with the known Hadamard input sequence. Here we show that employing the Hadamard time coding in the confocal surface plasmon interferometry enables us to (1) perform widefield imaging, (2) higher signal-to-noise compared to the beam scanning system, (3) high sensitivity, (4) good spatial resolution and (5) more stable compared to the confocal surface plasmon microscope.

## 1 INTRODUCTION

Doctors and biomedical scientists have been facing more challenging diseases in these recent years. Bacteria, germs, and viruses have become more tolerant and resistant to chemicals and antibiotic drugs (Boolchandani, D'Souza, & Dantas, 2019). Fever and flu, such as COVID-19, have been severe healthcare issues worldwide (Fricker Jr & Rigdon, 2018; Organization, 2020). Not only that, but there are also symptoms and illnesses related to the aging society; of course, one of the majority is neurodegenerative diseases (Barnham, Masters, & Bush, 2004), such as Alzheimer's disease. The number of patients diagnosed with the disease is increasing yearly, and there is still no promising and reliable early-stage diagnostic tool (Venazzi et al., 2018). There is an increasing demand for highly sensitive biosensors to tackle such situations and, of course, for early-stage diagnosis of server illnesses. From the literature review, the following are the critical demands for next-generation diagnostic tools, which can be summarized as:

1. In vitro imaging capability to understand the physical interactions between cells, drugs, and

morphology of mutant bacteria or viruses (Xiao, Parchur, Gilbertson, & Zhou, 2018).

2. Biosensing capability, besides imaging capability ability to identify the presence of genes or proteins, is also the key. This character is where fluorescence labeling plays a crucial role (Ounkomol, Seshamani, Maleckar, Collman, & Johnson, 2018).
3. Highly sensitive, one of the hot topics in biomedical sensors is single molecule detection due to the high demand in the healthcare sector (Zanchetta, Lanfranco, Giavazzi, Bellini, & Buscaglia, 2017).
4. Quantitative imaging not only gives out imaging, but it needs to be also able to perform a quantitative measurement, such as showing interaction strengths and binding kinetics (Guerri et al., 2018).
5. High throughput screening different kinds of binding arrays (Songa & Okonkwo, 2016).
6. Label-free, although fluorescence techniques have their unique advantage, there are key issues in those techniques, including photobleaching and phototoxicity. They may also not represent the natural behavior of the specimen due to the

perturbation of the considerable molecular weight of the fluoresce dyne (Zanchetta et al., 2017).

- Automatic feedback control system and self-calibration (Hameed, Alrayk, & Obayya, 2016), for example, automatic z-control for long-period imaging, reference channel in the measurement of binding kinetics.

Scientists and engineers are trying to provide feasible solutions to medical needs. One of the promising candidates that have been of interest to the science community and healthcare sensor manufacturers is surface plasmon resonance (SPR).

SPR is a confined electromagnetic wave propagating along the surface of noble metals, such as gold (Au), silver (Ag), and copper (Cu). The SPR is sensitive to molecules and substances that bind to the metal surface and appears as the change in wave vector  $k_{sp}$  of the surface plasmons (SP) (Nguyen, Park, Kang, & Kim, 2015). The SPR measurement is carried out for biosensing applications using a uniform layer of thin gold film 50nm thick coated on a high refractive index prism or glass substrate. A p-polarized light with sufficient light momentum illuminates the gold sensor from the glass side, as shown in Fig.1. The analyte and binding site are on the other side of the gold, the so-called Kretschmann configuration.

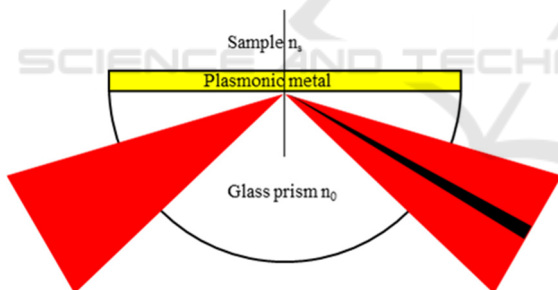


Figure 1: Kretschmann configuration.

No labeling agent is required in such measurement, and the SPR measurement is a label-free technique. A dark band dip appears on the reflectance curve, as shown in Fig.1. This is evidence of SPR coupling, as the presence of the dark band is due to the SPR loss mechanisms in the SPR coupling process (Pechprasarn, Chow, & Somekh, 2018). When the analyte binds to the binding site, this dark band dip moves to a higher wave vector position. Since the SPR is an electromagnetic wave propagation and, of course, phase detection is also possible.

It has been very well established that phase detection gives better sensitivity (Ho et al., 2006;

Huang, Ho, Kong, & Kabashin, 2012) due to the sharper phase response of the phase curve compared to the intensity measurement. However, it does require an interferometric system.

The interferometric system usually requires well-controlled experimental conditions, such as temperature control and vibration isolation. This paper will demonstrate how the proposed widefield, confocal surface plasmon can overcome the variations by employing time-coded illumination using the Hadamard code. The Hadamard sequence is an orthogonal sequence enabling a widefield, confocal imaging capability.

## 2 MATERIALS AND METHODS

### 2.1 Optical Microscope Simulation

We address the issues of scanning confocal surface plasmon interferometric system by employing a rotating diffuser for incoherent illumination and a digital micromirror device (DMD) as shown in Fig.2. The DMD is for controlling the pattern of image plane illumination using Hadamard sequence intensity coding. The incoherent illumination ensures no interference effect between any close point spread functions.

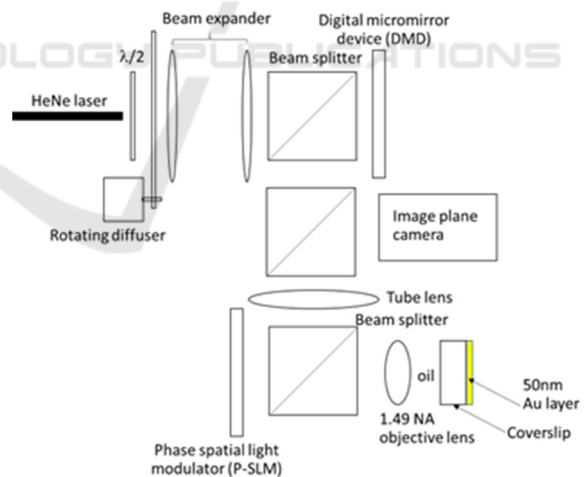


Figure 2: Schematic diagram of SPR microscope with digital micromirror device for image plane illumination control.

An example of 64x64 Hadamard sequences is shown in Fig.3. It is essential to point out that Hadamard sequences are a series of orthogonal codes consisting of -1 and 1. Each row of the Hadamard matrix can be employed to code an individual pixel on the DMD chip.

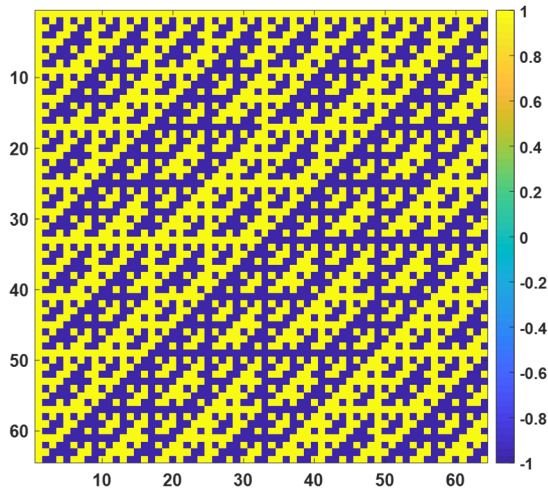


Figure 3: A 64x64 Hadamard matrix.

One significant difference between Hadamard's code and the optical illumination is that the camera in the microscope system can only detect light intensity. Therefore, the Hadamard code in this research is adjusted to 0 and 1, as shown in Fig.3a here, called  $\bar{H}$ . Moreover, the conventional Hadamard with -1 and 1 coding, as shown in Fig.3b, is called  $H$ .

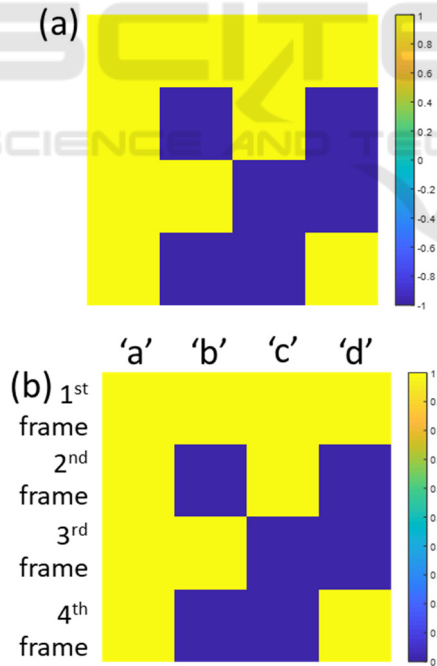


Figure 4: Shows (a) the conventional Hadamard  $H$  with -1 and 1 coding for a 4 by 4 matrix and (b) the adjusted Hadamard  $H$  with 0 and 1 coding for a 4 by 4 matrix.

To demonstrate the feasibility of the proposed method, let us assume that we would like to measure

confocal responses of 4 measurement positions in the image plane  $I_a, I_b, I_c$  and  $I_d$ , respectively. These 4 points in the image plane are separated by arbitrary distances and directions leading to different crosstalk. Let  $\alpha_{ab}$  is the crosstalk from point 'b' leaking into point 'a'. Therefore, there are 12 crosstalk terms  $\alpha_{ab}, \alpha_{ba}, \alpha_{ac}, \alpha_{ca}, \alpha_{ad}, \alpha_{da}, \alpha_{bc}, \alpha_{cb}, \alpha_{bd}, \alpha_{db}, \alpha_{cd}$  and  $\alpha_{dc}$  for the 4 points.

An essential property of the orthogonal matrix is that:

$$H^T \times H = nI \quad (1)$$

Where  $H^T$  is the transpose of the Hadamard matrix

$H$  is the Hadamard matrix

$n$  is the Hadamard matrix dimension

$I$  is the identity matrix

These are applicable to reconstruct the reflectance for each spatial position coded using the Hadamard sequence as:

$$H^T \times (H \cdot R) = n(I \cdot R) \quad (2)$$

Where  $R$  is the reflectance corresponding to each spatial position in the image plane.

Having mentioned that it is impossible to capture -1 code, this is replaced by 0 in this research. The orthogonal code cannot correctly cancel out all the crosstalk. Here we propose a set of the simultaneous equation to reconstruct the correct intensity for each spatial position in the image plane without crosstalk from the other illuminating pixels. In the case of the 4x4 pixel, the  $\bar{H} \cdot R$  can be expressed as:

$$\bar{H} \cdot R = \begin{bmatrix} I_a + \alpha_{ab} + \alpha_{ac} + \alpha_{ad} & I_b + \alpha_{ba} + \alpha_{bc} + \alpha_{bd} & I_c + \alpha_{ca} + \alpha_{cb} + \alpha_{cd} & I_d + \alpha_{da} + \alpha_{db} + \alpha_{dc} \\ I_a + \alpha_{ab} & \alpha_{ba} + \alpha_{bc} & I_c + \alpha_{ca} & \alpha_{da} + \alpha_{dc} \\ I_a + \alpha_{ad} & \alpha_{ba} + \alpha_{bd} & \alpha_{ca} + \alpha_{cd} & I_d + \alpha_{da} \end{bmatrix} \quad (3)$$

$$H^T \times (\bar{H} \cdot R) = \begin{bmatrix} 4I_a + 2\alpha_{ab} + 2\alpha_{ac} + 2\alpha_{ad} & 2I_b + 4\alpha_{ba} + 2\alpha_{bc} + 2\alpha_{bd} & 2I_c + 4\alpha_{ca} + 2\alpha_{cb} + 2\alpha_{cd} & 2I_d + 4\alpha_{da} + 2\alpha_{db} + 2\alpha_{dc} \\ 2\alpha_{ab} & 2I_b & 2\alpha_{cb} & 2\alpha_{db} \\ 2\alpha_{ac} & 2\alpha_{bc} & 2I_c & 2\alpha_{dc} \\ 2\alpha_{ad} & 2\alpha_{bd} & 2\alpha_{cd} & 2I_d \end{bmatrix} \quad (4)$$

The diagonal elements and the first column of the matrix shown in Equation (4) allow us to determine  $I_a, I_b, I_c$  and  $I_d$ . The other elements also enable us to determine all the crosstalk terms.

The reflectance point spread function of 1.49NA with a linearly polarized laser beam at 633 nm was simulated for a 50nm plasmonic gold sample coated on a standard coverslip to demonstrate the proposed method. The sample is then illuminated using the

Hadamard code in Fig.4b, in which each row in Fig.4b represents a camera frame. Assuming that the intensity of the reflectance point spread function is 1 for each position in the image plane. Fig.5 shows the 4 simulated camera frames corresponding to the Hadamard sequences in Fig.4b. Fig.6a shows the  $\bar{H} \bullet R$  matrix and Fig.6b shows the  $H^T \times (\bar{H} \bullet R)$  matrix calculated using Equation (3) and Equation (4), respectively. The reflectance of the 4 measurement positions can then be determined from the diagonal matrix and the first column of the  $H^T \times (\bar{H} \bullet R)$  matrix and found to be all 1 as defined in this example.

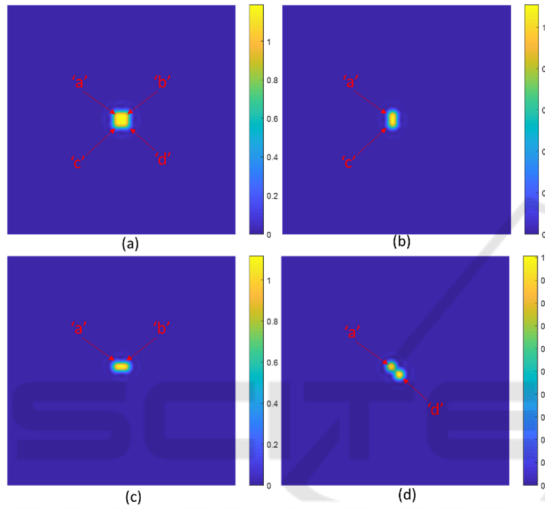


Figure 5: Simulated reflectance from a 50 nm thick gold sensor using (a) the 1<sup>st</sup> frame of the adjusted Hadamard code in Fig.4b, (b) the 2<sup>nd</sup> frame of the adjusted Hadamard code in Fig.4b, (c) the 3<sup>rd</sup> frame of the adjusted Hadamard code in Fig.4b and (d) the 4<sup>th</sup> frame of the adjusted Hadamard code in Fig.4b.

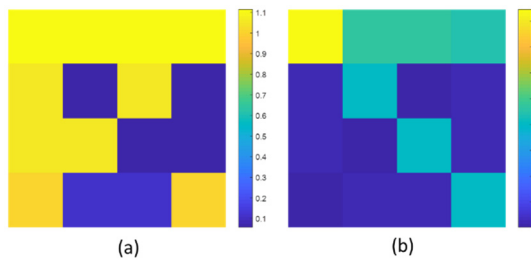


Figure 6: Shows (a)  $\bar{H} \bullet R$  and (b)  $H^T \times (\bar{H} \bullet R)$  calculated using Equation (3) and Equation (4).

## 2.2 Optical Simulation Parameters

The system in Fig. 2 consists of a linearly polarized laser at 633 nm wavelength (HeNe). The objective lens is an oil immersion objective lens 1.49NA with

x100 magnification. The plasmonic sensor is a uniform sensor made of 50nm gold coated on a standard coverslip with 0.17mm thickness. The refractive index of the coverslip is  $n_{\text{glass}}$  of 1.52, and the refractive index of the immersion oil noil of 1.52. The complex refractive index of gold at 633 nm wavelength is  $n_{\text{gold}}$  of  $0.1834+3.4332i$  (Johnson & Christy, 1972). The gold sensor is coated with 10 nm thick Bovine Serum Albumin (BSA) protein with a refractive index of 1.4 (Chow, Pechprasarn, Meng, & Somekh, 2016). A water environment with a refractive index of 1.33 backs the sensor.

## 3 RESULTS

This section provides simulation results to demonstrate how the widefield SPR phase measurement can be achieved. The following is a list of optical and physical parameters computed in the simulation. These parameters can be realized under standard optical experimental conditions. The system configuration is the same as shown in Fig.2. The back focal response (BFP) of the microscope objective, as shown in Fig.7, is calculated by Fresnel equations and a transfer matrix approach computed in Matlab. Fig.7a shows the intensity response of the BFP, and Fig.7b shows the phase response of the corresponding BFP.

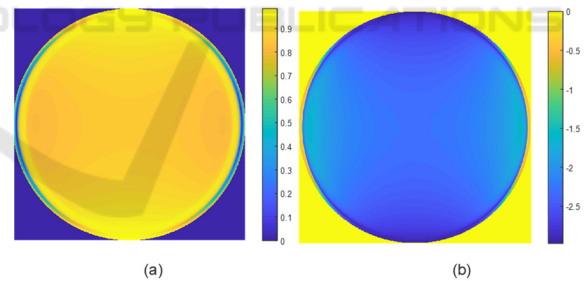


Figure 7: (a) Intensity response of the BFP and (b) phase response of the simulated BFP.

The microscope point spread function for different  $z$  defocus ranging from -6 microns to 2 microns, as shown in Fig.8, was then computed by multiplying defocus phase function  $\exp(i2kz\cos\theta)$  to the BFP response, where  $k$  is the wave vector given by  $2\pi n_0/\lambda$ .  $\theta$  is the incident angle, and  $z$  is the axial defocus distance of the sample stage.

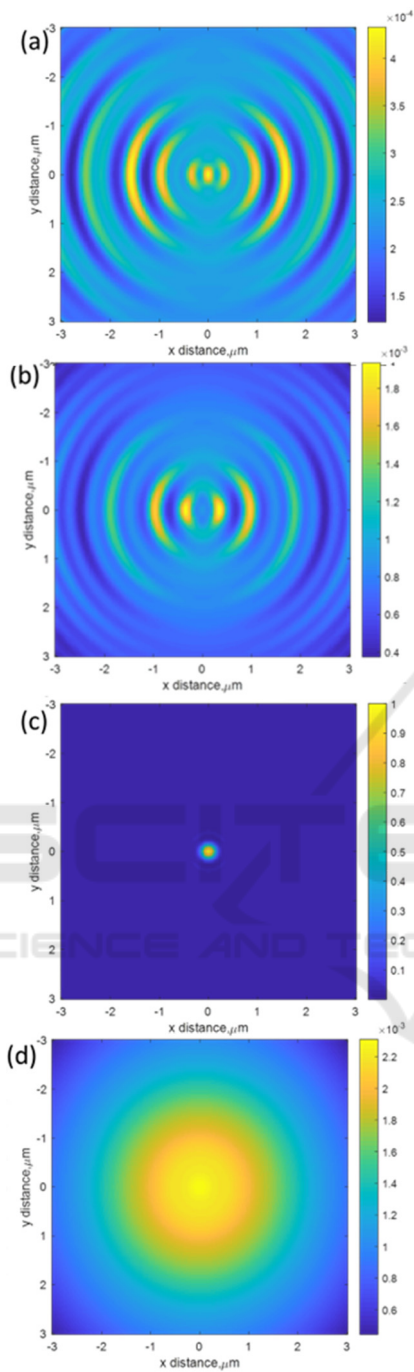


Figure 8:  $V(z)$  responses for (a)  $z$  of  $-6$  microns (b)  $z$  of  $-3$  microns (c)  $z$  of  $0$  microns and (d)  $z$  of  $2$  microns.

The reflectance of 4 measurement positions separated by 100 nm was then computed by convolution calculation, as shown in Fig.9. The adjusted Hadamard coding shown in Fig.4b was then applied to the 4 measurement positions. Note that the 4 measurement positions were purely for illustration

here; the proposed method can be applicable with much larger pixels.

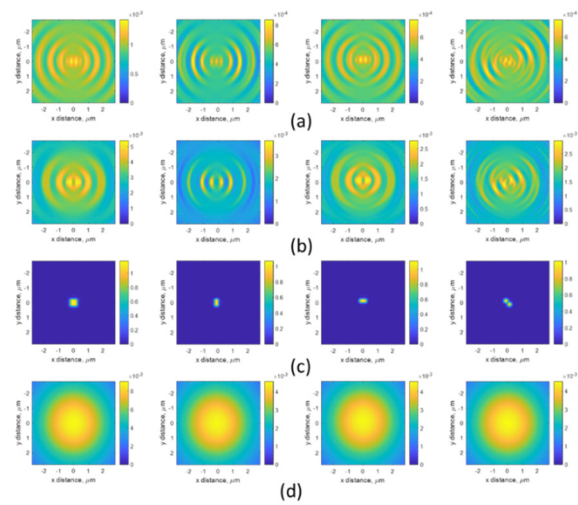


Figure 9: (a) Reflectance at  $z$  of  $-6$  microns, (b) reflectance at  $z$  of  $-3$  microns, (c) reflectance at  $z$  of  $0$  microns, and (d) reflectance at  $z$  of  $2$  microns.

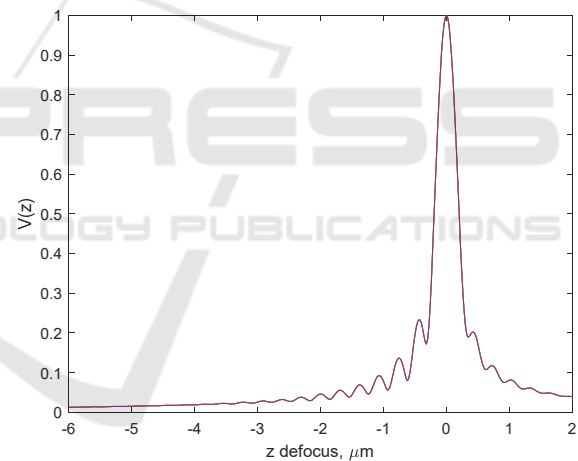


Figure 10:  $V(z)$  confocal responses of the 4 measurement positions. Note that the 4  $V(z)$  curves are the same.

Equation (4) was then applied to separate the crosstalk effect. The  $V(z)$  confocal responses (Zhang, Pechprasarn, & Somekh, 2012; Zhang, Pechprasarn, Zhang, & Somekh, 2012) corresponding to the 4 measurement positions are shown in Fig.10. The  $V(z)$  curves of the 4 measurement positions are successfully reconstructed. They all have the same amplitude, shape, and ripple period. Note that the results in Fig.8 and Fig.9 were displayed in intensity, whereas the  $V(z)$  curves in Fig.10 were plotted in the square root of intensity.

## 4 CONCLUSION

Here, we have proposed and analyzed an optical widefield, confocal surface plasmon configuration based on time-coded illumination. It is more robust and has a better signal-to-noise ratio than a conventional scanning confocal surface plasmon microscope allowing multiple confocal scanning point spread functions to scan over the sample simultaneously. The crosstalk between the overlapping point spread functions can be suppressed and reconstructed using the property of orthogonal coding in the image plane of the microscope objective. The proposed method can be integrated with standard microscope systems to provide widefield, confocal imaging.

## ACKNOWLEDGEMENTS

The authors would like to acknowledge the Research Institute of Rangsit University for supporting the research; and the College of Biomedical Engineering, Rangsit University, for the computing power and research laboratory used in this work.

## REFERENCES

- Barnham, K. J., Masters, C. L., & Bush, A. I. (2004). Neurodegenerative diseases and oxidative stress. *Nature reviews Drug discovery*, 3(3), 205-214.
- Boolchandani, M., D'Souza, A. W., & Dantas, G. (2019). Sequencing-based methods and resources to study antimicrobial resistance. *Nature Reviews Genetics*, 20(6), 356-370.
- Chow, T. W., Pechprasarn, S., Meng, J., & Somekh, M. G. (2016). Single shot embedded surface plasmon microscopy with vortex illumination. *Optics Express*, 24(10), 10797-10805.
- Fricker Jr, R. D., & Rigdon, S. E. (2018). Disease surveillance: Detecting and tracking outbreaks using statistics. *Chance*, 31(2), 12-22.
- Guerra, S., Mercatelli, D., Gómez, M. P. A., Napoli, A., Battista, G., Guglielmi, G., & Bazzocchi, A. (2018). Quantitative imaging techniques for the assessment of osteoporosis and sarcopenia. *Quantitative imaging in medicine and surgery*, 8(1), 60.
- Hameed, M. F. O., Alrayk, Y. K., & Obayya, S. (2016). Self-calibration highly sensitive photonic crystal fiber biosensor. *IEEE photonics journal*, 8(3), 1-12.
- Ho, H., Law, W. C., Wu, S., Liu, X., Wong, S., Lin, C., & Kong, S. (2006). Phase-sensitive surface plasmon resonance biosensor using the photoelastic modulation technique. *Sensors and Actuators B: Chemical*, 114(1), 80-84.
- Huang, Y., Ho, H. P., Kong, S. K., & Kabashin, A. V. (2012). Phase - sensitive surface plasmon resonance biosensors: methodology, instrumentation and applications. *Annalen Der Physik*, 524(11), 637-662.
- Johnson, P. B., & Christy, R.-W. (1972). Optical constants of the noble metals. *Physical review B*, 6(12), 4370.
- Nguyen, H. H., Park, J., Kang, S., & Kim, M. (2015). Surface plasmon resonance: a versatile technique for biosensor applications. *Sensors*, 15(5), 10481-10510.
- Organization, W. H. (2020). Coronavirus disease 2019 (COVID-19): situation report, 51.
- Ounkomol, C., Seshamani, S., Maleekar, M. M., Collman, F., & Johnson, G. R. (2018). Label-free prediction of three-dimensional fluorescence images from transmitted-light microscopy. *Nature methods*, 15(11), 917-920.
- Pechprasarn, S., Chow, T. W., & Somekh, M. G. (2018). Application of confocal surface wave microscope to self-calibrated attenuation coefficient measurement by Goos-Hänchen phase shift modulation. *Scientific reports*, 8(1), 1-14.
- Songa, E. A., & Okonkwo, J. O. (2016). Recent approaches to improving selectivity and sensitivity of enzyme-based biosensors for organophosphorus pesticides: A review. *Talanta*, 155, 289-304.
- Venazzi, A., Swardfager, W., Lam, B., Siqueira, J. d. O., Herrmann, N., & Cogo-Moreira, H. (2018). Validity of the QUADAS-2 in assessing risk of bias in Alzheimer's disease diagnostic accuracy studies. *Frontiers in psychiatry*, 9, 221.
- Xiao, L., Parchur, A. K., Gilbertson, T. A., & Zhou, A. (2018). SERS-fluorescence bimodal nanoprobe for in vitro imaging of the fatty acid responsive receptor GPR120. *Analytical Methods*, 10(1), 22-29.
- Zanchetta, G., Lanfranco, R., Giavazzi, F., Bellini, T., & Buscaglia, M. (2017). Emerging applications of label-free optical biosensors. *Nanophotonics*, 6(4), 627-645.
- Zhang, B., Pechprasarn, S., & Somekh, M. G. (2012). Surface plasmon microscopic sensing with beam profile modulation. *Optics Express*, 20(27), 28039-28048.
- Zhang, B., Pechprasarn, S., Zhang, J., & Somekh, M. G. (2012). Confocal surface plasmon microscopy with pupil function engineering. *Optics Express*, 20(7), 7388-7397.